Astronomy & Astrophysics

An advective solar-type dynamo without the α effect[⋆]

N. Seehafer[1] and V. V. Pipin[2]

[1] Institut für Physik und Astronomie, Universität Potsdam, Karl-Liebknecht-Str. 24/25, 14476 Potsdam, Germany
e-mail: seehafer@uni-potsdam.de
[2] Institute for Solar-Terrestrial Physics, Siberian Division of the Russian Academy of Sciences, 664033 Irkutsk, Russia
e-mail: pip@iszf.irk.ru

ABSTRACT

Context. Most solar and stellar dynamo models use the $\alpha\Omega$ scenario where the magnetic field is generated by the interplay between differential rotation (the Ω effect) and a mean electromotive force due to helical turbulent convection flows (the α effect). There are, however, turbulent dynamo mechnisms that may complement the α effect or may be an alternative to it.
Aims. We investigate models of solar-type dynamos where the α effect is completely replaced by two other turbulent dynamo mechanisms, namely the $\mathbf{\Omega} \times \mathbf{J}$ effect and the shear-current effect, which both result from an inhomogeneity of the mean magnetic field.
Methods. We studied axisymmetric mean-field dynamo models containing differential rotation, the $\mathbf{\Omega} \times \mathbf{J}$ and shear-current effects, and a meridional circulation. The model calculations were carried out using the rotation profile of the Sun as obtained from helioseismic measurements and radial profiles of other quantities according to a standard model of the solar interior.
Results. Without meridional flow, no satisfactory agreement of the models with the solar observations can be obtained. With a sufficiently strong meridional circulation included, however, the main properties of the large-scale solar magnetic field, namely, its oscillatory behavior, its latitudinal drift towards the equator within each half cycle, and its dipolar parity with respect to the equatorial plane, are correctly reproduced.
Conclusions. We have thereby constructed the first mean-field models of solar-type dynamos that do not use the α effect.

Key words. stars: magnetic fields – Sun: magnetic fields – magnetohydrodynamics (MHD)

1. Introduction

The standard dynamo model for the Sun and stars is the $\alpha\Omega$ model where, within the framework of mean-field magnetohydrodynamics, the magnetic field is produced by an interplay between differential rotation (the Ω effect) and the collective action of turbulent cyclonic convection flows, known as the α effect (Parker 1955, 1979; Steenbeck et al. 1966; Krause & Rädler 1980). The α effect is here responsible for generating the poloidal component of the large-scale magnetic field (LSMF), whose toroidal component is mainly generated by the the Ω effect. The model is often supplemented with meridional flows, leading to so-called flux-transport dynamos (e.g., Choudhuri et al. 1995; Küker et al. 2001; Rempel 2006; Dikpati & Gilman 2007). The meridional flows may transport toroidal magnetic flux toward the equator and their speed may determine the cycle period, thus allowing us to bypass a number of problems connected with the α effect and $\alpha\Omega$ dynamos, as, for instance, that, in the case of the Sun, the obtained cycle periods are generally too short and the magnetic activity is not sufficiently concentrated at low latitudes (see, e.g., Ossendrijver 2003; Rüdiger & Hollerbach 2004; Brandenburg & Subramanian 2005a).

In mean-field magnetohydrodynamics, the influence of the turbulence on the LSMF is expressed by the mean turbulent electromotive force (MEMF), $\mathcal{E} = \langle \mathbf{u} \times \mathbf{b} \rangle$, where $\mathbf{u}$ and $\mathbf{b}$ are the fluctuating parts of the velocity and magnetic field and angular brackets denote averages. The by far best known contribution to $\mathcal{E}$ is provided by the α effect, namely, a turbulent electromotive force $\alpha\langle \mathbf{B} \rangle$, with α denoting a (symmetric) tensorial factor of

proportionality and $\langle \mathbf{B} \rangle$ the LSMF. However, there are other turbulent dynamo mechanisms besides the α effect. Two of them are the $\mathbf{\Omega} \times \mathbf{J}$ effect (Rädler 1969; Stix 1976) and the shear-current or $\mathbf{W} \times \mathbf{J}$ effect (Rogachevskii & Kleeorin 2003, 2004); $\mathbf{\Omega}$ is here the angular velocity of the stellar rotation, $\mathbf{J} = \nabla \times \langle \mathbf{B} \rangle / \mu_0$ the large-scale electric-current density, and $\mathbf{W} = \nabla \times \mathbf{V}$ the large-scale vorticity, $\mathbf{V}$ denoting the large-scale velocity. Both these effects result from an inhomogeneity of the LSMF, in contrast to the α effect, which also works with a homogeneous $\langle \mathbf{B} \rangle$ (that is to say, for calculating the α effect, $\langle \mathbf{B} \rangle$ may be considered as homogeneous on the scale of the fluctuations).

In the commonly used representation of the MEMF on the basis of symmetry considerations (see Rädler 1980; Krause & Rädler 1980; Rädler 2000; Rädler et al. 2003), the $\mathbf{\Omega} \times \mathbf{J}$ and shear-current effects represent contributions to the δ term, a term of the form $\mathcal{E}_\delta = \delta \times (\nabla \times \langle \mathbf{B} \rangle)$, where δ is a vector. Since $\mathcal{E}_\delta \cdot \mathbf{J} = 0$, the effects described by this term cannot bring energy into the mean magnetic field and, thus, cannot lead to working dynamos when acting alone. These effects have been investigated little in the context of solar and stellar dynamos. For a recent study of the possible role of the $\mathbf{\Omega} \times \mathbf{J}$ effect when acting together with the α effect and differential rotation in a spherical shell, or when acting together with another part of the MEMF, not included in dynamo studies before, in a rigidly rotation full sphere, see Pipin & Seehafer (2009), where an illustration of the physical mechanism behind the $\mathbf{\Omega} \times \mathbf{J}$ effect also may be found; the mechanism of the shear-current effect is very similar to that of the $\mathbf{\Omega} \times \mathbf{J}$ effect.

In this paper, we consider mean-field dynamo models in the geometry of a spherical shell, as appropriate for solar-type stars, where the α effect is completely omitted. Instead, the $\mathbf{\Omega} \times \mathbf{J}$ and

---

[⋆] Appendices A and B are only available in electronic form at http://www.aanda.org

shear-current effects serve as turbulent dynamo mechanisms. In nearly all mean-field dynamo studies, the effective strengths of the different physical ingredients are controlled by freely varied dimensionless parameters; in the case of dynamo effects, e.g., the α effect, these are usually referred to as dynamo numbers. This reflects our present knowledge of the physical processes in the convection zones of the Sun and stars. Realistic self-consistent numerical models of these processes and their interactions will remain out of reach for the foreseeable future. Given this situation, we deem it advisable to explore the potentials of turbulent dynamo effects other than the α effect.

Numerical evidence for turbulent dynamo effects has so far mainly been obtained from convection simulations in small (compared to the dimensions of a star) rectangular boxes (e.g., Brandenburg et al. 1990; Ossendrijver et al. 2001, 2002; Giesecke et al. 2005; Käpylä et al. 2006; Cattaneo & Hughes 2006; Hughes & Cattaneo 2008). Due to the assumption of a uniform mean magnetic field and other limitations, most of these studies could only find parts of the MEMF that are proportional to the LSMF, i.e., the α effect and turbulent pumping (a contribution to the MEMF of the form $\mathcal{E}_\gamma = \gamma \times \langle \boldsymbol{B} \rangle$, with γ denoting a vector; it leads to an advection of the mean magnetic field). Recently, however, Käpylä et al. (2009), who used a procedure referred to as the test field method (Schrinner et al. 2005, 2007) together with numerical simulations of turbulent convection with shear and rotation, were able to also identify the action of the combined $\boldsymbol{\Omega} \times \boldsymbol{J}$ and shear-current effects.

Here, we explore axisymmetric kinematic dynamo models containing the $\boldsymbol{\Omega} \times \boldsymbol{J}$ and shear-current effects, differential rotation, and meridional circulation. In calculating the MEMF we use analytical expressions derived by Pipin (2008) on the basis of a simplified version of the τ approximation (cf. Vainshtein & Kichatinov 1983; Brandenburg & Subramanian 2005a,b). We construct models with distributed dynamo action in the bulk of the convection zone, rather than in the overshoot layer at the bottom of the convection zone. The model calculations are carried out using the rotation profile of the Sun as obtained from helioseismic measurements and radial profiles of other quantities according to a standard model of the solar interior.

The remainder of the paper is organized as follows: in Sect. 2 we describe our dynamo model, as well as the used numerical procedure (some benchmark tests for our computer code are presented in Appendix A). Then, in Sect. 3, we present the obtained results. In Sect. 4, we draw conclusions and discuss our results.

2. Model and numerical procedure

The axisymmetric LSMF is written in the usual way as the sum of a poloidal and a toroidal part,

$$\langle \boldsymbol{B} \rangle = \nabla \times \frac{A \boldsymbol{e}_\phi}{r \sin \theta} + B \, \boldsymbol{e}_\phi \,, \tag{1}$$

where $A(r, \theta, t)$ (the flux function for the poloidal field) and $B(r, \theta, t)$ (the toroidal field component) are scalar functions of radius, r, colatitude, θ, and time, t, and $\boldsymbol{e}_\phi$ is the unit vector in the direction of the azimuthal coordinate, ϕ. The mean-field induction equation then takes the form

$$\frac{\partial A}{\partial t} = r \sin \theta \, \mathcal{E}_\phi - \frac{U_\theta}{r} \frac{\partial A}{\partial \theta} - U_r \frac{\partial A}{\partial r} \,, \tag{2}$$

$$\frac{\partial B}{\partial t} = \frac{1}{r} \frac{\partial (\Omega, A)}{\partial (r, \theta)} + \frac{1}{r} \left(\frac{\partial r (\mathcal{E}_\phi - U_r B)}{\partial r} - \frac{\partial (\mathcal{E}_r + U_\theta B)}{\partial \theta} \right) \,, \tag{3}$$

where the effects of the large-scale flows enter through the differential-rotation rate, $\Omega(r, \theta) = |\boldsymbol{\Omega}(r, \theta)|$, and the components of the meridonal flow, U_r and U_θ.

To calculate the MEMF, whose effects appear through the components of $\boldsymbol{\mathcal{E}}$ in Eqs. (2) and (3), we modify the expressions given in Pipin & Seehafer (2009) by completely omitting the α effect but including, in addition to the $\boldsymbol{\Omega} \times \boldsymbol{J}$ effect, isotropic and anisotropic turbulent diffusion, and turbulent pumping, now also the shear-current effect. The contribution of this to the MEMF is to linear order, i.e., for a weak mean magnetic field, as well as neglecting the effect of the Coriolis force, given by (Pipin 2008)

$$\begin{aligned} \mathcal{E}_i^{(W)} &= \varepsilon_{inm} \Big\{ C_1 \overline{V}_{\text{lm}} \overline{B}_{\text{nl}} + C_2 \overline{B}_{\text{nl}} \overline{V}_{\text{ml}} + C_3 \overline{V}_{lm} \overline{B}_{\text{ln}} \\ &\quad + C_4 \overline{B}_{\text{ln}} \overline{V}_{\text{ml}} \Big\} \left\langle u^{(0)2} \right\rangle \tau_c^2 \,, \end{aligned} \tag{4}$$

where tensor notation and the summation convention have been used. $\overline{B}_{ij} = \partial \langle B_i \rangle / \partial x_j$ is the gradient tensor of the mean magnetic field and $\overline{V}_{ij}$ a corresponding quantity for the differential rotation, namely, $\overline{V}_{ij} = \partial V_i / \partial x_j$, with $\boldsymbol{V} = r \sin \theta (\Omega - \Omega_0) \boldsymbol{e}_\phi$ being the rotational velocity, defined in a reference frame that rotates with angular velocity Ω_0, the rigid-body rotation rate of the core (encountered at midlatitudes through the convection zone). $\boldsymbol{u}^{(0)}$ is a small-scale or turbulent convective background velocity as present in the absence of rotation and a mean magnetic field, τ_c the correlation time of $\boldsymbol{u}^{(0)}$, and $C_1 = (\varepsilon - 3/5)/6$, $C_2 = (\varepsilon - 1)/5$, $C_3 = (1 + \varepsilon)/15$, and $C_4 = -(7\varepsilon + 11)/30$ are constants; $\varepsilon = \sqrt{\langle b^{(0)2} \rangle} / (u_c \sqrt{\mu_0 \rho})$ is the square root of the prescribed ratio between the energies of a fluctuating magnetic background field $b^{(0)}$, assumed to be generated by a small-scale dynamo (which is fully independent of the mean magnetic field), and the background velocity field $\boldsymbol{u}^{(0)}$ ($u_c = \sqrt{\langle u^{(0)2} \rangle}$ is the rms value of the background velocity field and ρ the mass density).

In the following, we assume energy equipartition between the two background fields, i.e., $\varepsilon = 1$. Furthermore, only the azimuthal $\boldsymbol{\Omega} \times \boldsymbol{J}$ and shear-current effects are taken into account. This may be justified by the fact that the toroidal part of the solar LSMF is much stronger than the poloidal one. However, the remaining parts of the MEMF (isotropic and anisotropic turbulent diffusion, turbulent pumping) are included in all components. The components of the MEMF in spherical coordinates then become

$$\begin{aligned} \mathcal{E}_r &= -\tilde{\eta}_T \left\{ \frac{f_2^{(d)} + 2 f_1^{(a)} \sin^2 \theta}{r \sin \theta} \frac{\partial \sin \theta B}{\partial \theta} - \frac{f_1^{(a)} \sin 2\theta}{r} \frac{\partial r B}{\partial r} \right. \\ &\quad \left. + G \sin 2\theta f_1^{(a)} B \right\} , \end{aligned} \tag{5}$$

$$\begin{aligned} \mathcal{E}_\theta &= \tilde{\eta}_T \left\{ \frac{f_2^{(d)} + 2 f_1^{(a)} \cos^2 \theta}{r} \frac{\partial r B}{\partial r} - \frac{2 f_1^{(a)} \cos \theta}{r} \frac{\partial \sin \theta B}{\partial \theta} \right. \\ &\quad \left. - G \left(f_3^{(a)} + \cos 2\theta f_1^{(a)} \right) B \right\} , \end{aligned} \tag{6}$$

$$\begin{aligned} \mathcal{E}_\phi &= \tilde{\eta}_T \left\{ \frac{f_2^{(d)} + 2 f_1^{(a)}}{r} \left(\frac{1}{\sin \theta} \frac{\partial^2 A}{\partial r^2} + \frac{1}{r^2} \frac{\partial}{\partial \theta} \frac{1}{\sin \theta} \frac{\partial A}{\partial \theta} \right) \right. \\ &\quad + G \left(\frac{2 \cos \theta f_1^{(a)}}{r^2} \frac{\partial A}{\partial \theta} - \frac{f_1^{(a)} \cos^2 \theta + f_3^{(a)}}{r \sin \theta} \frac{\partial A}{\partial r} \right) \\ &\quad \left. + C_\delta^{(\Omega)} f_4^{(d)} \left(\cos \theta \frac{\partial B}{\partial r} - \frac{\sin \theta}{r} \frac{\partial B}{\partial \theta} \right) \right\} + \mathcal{E}_\phi^{(W)} \,, \end{aligned} \tag{7}$$

with $\mathcal{E}_\phi^{(W)}$ in Eq. (7) denoting the contribution of the shear-current effect, given by

$$
\begin{aligned}
\mathcal{E}_\phi^{(W)} &= \tilde{\eta}_T C_\delta^{(W)} f_4^{(d)} \left\{ \frac{11}{6} \left(\hat{\Omega} - 1 \right) \left(\cos\theta \frac{\partial B}{\partial r} - \frac{\sin\theta}{r} \frac{\partial B}{\partial \theta} \right) \right. \\
&\quad + \frac{1}{3} \sin\theta \frac{\partial \left(B, \hat{\Omega} \right)}{\partial (r, \theta)} \\
&\quad + \left. \frac{B}{6} \left(\cos\theta \frac{\partial \hat{\Omega}}{\partial r} - \frac{\sin\theta}{r} \frac{\partial \hat{\Omega}}{\partial \theta} \right) \right\}.
\end{aligned}
\tag{8}
$$

$f_1^{(a)}$, $f_3^{(a)}$, $f_2^{(d)}$, and $f_4^{(d)}$ denote functions of ε and the Coriolis number $\Omega^* = 2\Omega_0 \tau_c$ that are given in Appendix B, $G = (\partial/\partial r) \log \rho$ is the density scale factor, $\hat{\Omega} = \Omega/\Omega_0$, and $\tilde{\eta}_T = C_\eta \eta_T$, with $\eta_T = \left\langle u^{(0)2} \right\rangle \tau_c$. $C_\eta \leq 1$, $C_\delta^{(\Omega)} \leq 1$, $C_\delta^{(W)} \leq 1$ are parameters to control the relative strengths of different turbulence effects. C_η regulates the turbulence level, and $C_\delta^{(\Omega)}$ and $C_\delta^{(W)}$ weight the $\mathbf{\Omega} \times \mathbf{J}$ effect and the shear-current effect, respectively.

Currently, the dependence of the shear-current effect on the Coriolis number is unknown. Equation (4) has been derived disregarding the effect of the Coriolis force and is, thus, safely applicable only in the limit of slow rotation, $\Omega^* \ll 1$. But in the solar convection zone, in particular its deeper layers, the Coriolis number is large, $\Omega^* \gg 1$ (cf., e.g., Fig. 2 in Pipin & Seehafer 2009). To take this into account, we modulate the value of $\mathcal{E}_\phi^{(W)}$, given by Eq. (8), by the quenching function $f_4^{(d)}(\Omega^*)$ which also appears in the expression for the $\mathbf{\Omega} \times \mathbf{J}$ effect (penultimate term in Eq. (7), proportional to $C_\delta^{(\Omega)}$); additionally, the expression for the shear-current effect is normalized so as to give Eq. (4) in the limit of slow rotation, for which one finds $f_4^{(d)}(\Omega^*) \approx (1/5)\Omega^*$. Without such a quenching, i.e., directly applying Eq. (4), the shear-current effect would become unrealistically strong at the bottom of the convection zone.

In our numerical calculations we have used a dimensionless form of the equations, substituting $r = x R_\odot$ and $t \to \eta_0 t / R_\odot^2$, where $\eta_0 = 1.8 \times 10^9$ m^2/s is the maximum value of η_T in the convection zone; that is, length is measured in units of the solar radius and time is measured in units of the turbulent magnetic diffusion time, $T_D \approx 8.5$ yr. The integration domain is radially bounded by $x = 0.72$ and $x = 0.96$. The boundary conditions on the magnetic field are the usual approximate perfect-conductor conditions, i.e., $A = 0$, $\frac{\partial x B}{\partial x} = 0$, at the bottom boundary (Köhler 1973), and vacuum conditions, that is, $B = 0$ and a continuous match of the poloidal field component to an exterior potential field, at the top boundary.

The radial profiles of characteristic quantities of the turbulence, such as the rms value u_c and the correlation length and time, ℓ_c and τ_c, of the convective background velocity field, as well as the density stratification, were calculated on the basis of a standard model of the solar interior (Stix 2002), assuming the ratio of the correlation length to the pressure scale height (referred to as the mixing-length parameter) to be 1.6. The rotation profile as known from helioseismic measurements (Schou et al. 1998) is approximated by

$$
\Omega = \Omega_0 f(x, \theta),
\tag{9}
$$

with

$$
f(x, \theta) = \frac{1}{435} \left[435 + 51 (x - x_0) + 26\phi(x) \left(1 - 5\cos^2\theta \right) \right.
\tag{10}
$$

$$
\left. - 3.5 \left(1 - 14\cos^2\theta + 21\cos^4\theta \right) \right],
\tag{11}
$$

where

$$
\phi(x) = 0.5 \left\{ 1 + \tanh\left[50(x - x_0) \right] \right\}
\tag{12}
$$

and $x_0 = 0.71$ is the position of tachocline, situated below the bottom boundary of the integration domain.

A remark concerning our locating the lower boundary at $x = 0.72$ seems in order. Very often this boundary is placed at $x = 0.65$ (cf., e.g., Jouve et al. 2008). Then, however, some modeling of the tachocline is needed, where the differential rotation changes into rigid rotation in the radiative core. The physical parameters of this transition region are rather uncertain at the moment. Here, we consider a convection-zone dynamo model with distributed dynamo action in the bulk of the convection zone, where all physical parameters needed can be derived from helioseismic measurements and the standard model of the solar interior. There are other dynamo models where the dynamo just operates in the tachocline (a critical discussion of arguments for and against deep-seated and distributed dynamos is found in Brandenburg 2005).

The meridional flow, $\mathbf{U}$, is modeled in the form of two stationary circulation cells, one in the northern and one in the southern hemisphere, with poleward motion in the upper and equatorward motion in the lower part of the convection zone (for the theory of the meridional circulation see, e.g., Rempel 2005, 2006; Miesch et al. 2008; Brun & Rempel 2009). The condition of mass conservation, $\nabla \cdot (\rho \mathbf{U}) = 0$, is ensured by a stream-function representation of $\rho \mathbf{U}$ (cf., e.g., Bonanno et al. 2002), so that

$$
\mathbf{U} = \frac{1}{\rho} \nabla \times \frac{\psi \mathbf{e}_\phi}{x \sin\theta} = \frac{1}{\rho} \nabla \psi \times \frac{\mathbf{e}_\phi}{x \sin\theta}.
\tag{13}
$$

The stream function, ψ, is written as

$$
\psi(x, \theta) = u_0 \hat{\psi}(x, \theta),
\tag{14}
$$

with u_0 denoting the maximum amplitude of $\mathbf{U}$, which is treated as a free paramter. Our choice for $\hat{\psi}(x, \theta)$ is

$$
\begin{aligned}
\hat{\psi}(x, \theta) &= c_0 \sin^2\theta \cos\theta \, T(x), \\
c_0 &= \left(\max \left| \frac{1}{\rho} \nabla \times \frac{\sin^2\theta \cos\theta \, T(x) \, \mathbf{e}_\phi}{x \sin\theta} \right| \right)^{-1},
\end{aligned}
\tag{15}
$$

where the function $T(x)$ is selected such that the top and bottom boundaries are impenetrable and stress-free (free of tangential stresses), that is (see, e.g., Batchelor 1967),

$$
U_x = 0, \quad \frac{\partial U_x}{\partial \theta} + x \frac{\partial U_\theta}{\partial x} - U_\theta = 0 \quad \text{at } x = x_t, \, x = x_b,
\tag{16}
$$

where x_t and x_b are the outer and inner radius, respectively, of the considered spherical shell. Using

$$
U_x = \frac{u_0 c_0 \left(3\cos^2\theta - 1 \right) T}{\rho x^2}, \quad U_\theta = -\frac{u_0 c_0 \sin\theta \cos\theta}{\rho x} \frac{dT}{dx},
\tag{17}
$$

as follows from Eqs. (13)–(15), the boundary conditions given by Eq. (16) take the form

$$
T = 0, \quad x \frac{d}{dx} \frac{1}{\rho x} \frac{dT}{dx} - \frac{1}{\rho x} \frac{dT}{dx} = 0 \quad \text{at } x = x_t, \, x = x_b
\tag{18}
$$

and are satisfied with

$$
T(x) = P_2(\xi) + c_1 \left[P_3(\xi) - \xi \right] + c_2 \left[P_4(\xi) - 1 \right] - 1,
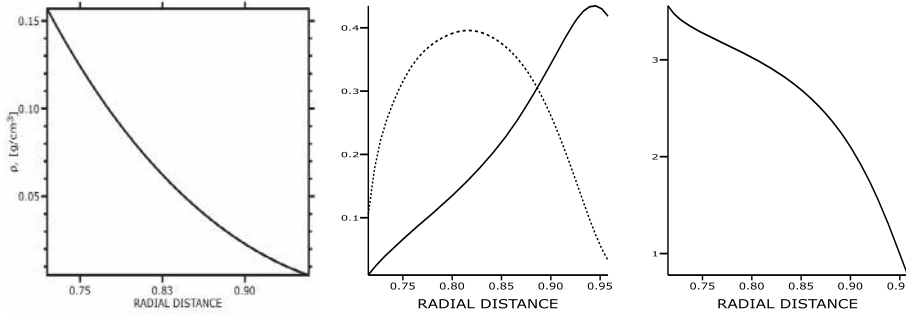\tag{19}
$$

Fig. 1. Radial profiles of model quantities. *Left*: mass density. *Middle*: isotropic ($\eta_T f_2^{(d)}(\Omega^*)$, solid line) and anisotropic ($2\eta_T f_1^{(a)}(\Omega^*)$, dashed line) turbulent magnetic diffusivities in units of η_0. *Right*: effective strength of the $\mathbf{\Omega} \times \mathbf{J}$ effect, $f_4^{(d)}(\Omega^*) / \left(f_2^{(d)}(\Omega^*) + 2f_1^{(a)}(\Omega^*) \right)$.
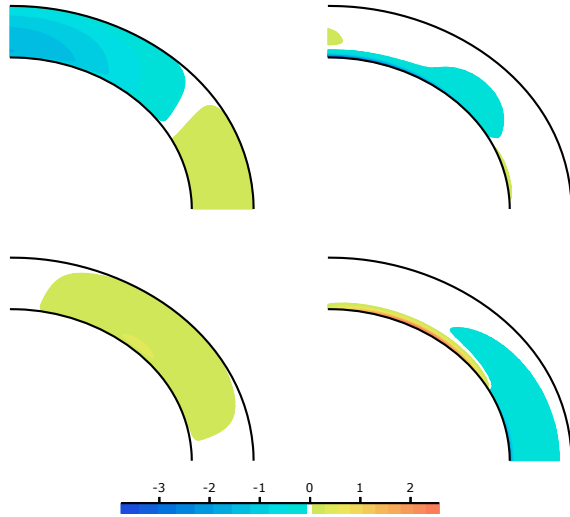

Fig. 3. The large-scale flows. *Left panel*: contours of the rotation rate Ω *(left)* and streamlines of the meridional flow, $\mathbf{U}$, i.e., contours of its stream function, ψ *(right)*. *Right panel*: radial profile of the component U_θ of the meridional flow at a latitude of 45° (in m/s).

Fig. 2. Effective strengths of the contributions to the shear-current effect as given by Eq. (8): $(11/6)(\hat{\Omega} - 1)N$ *(top left)*, $(1/6)(\cos\theta\, \partial\hat{\Omega}/\partial x - (\sin\theta/x)\, \partial\hat{\Omega}/\partial\theta)N$ *(top right)*, $(1/3)\sin\theta\left(\partial\hat{\Omega}/\partial\theta\right)N$ *(bottom left)*, and $-(1/3)\sin\theta(\partial\hat{\Omega}/\partial r)N$ *(bottom right)*, with $N = f_4^{(d)}(\Omega^*)/(f_2^{(d)}(\Omega^*) + 2f_1^{(a)}(\Omega^*))$.

where

$$\xi = \frac{2x - (x_t + x_b)}{x_t - x_b} \qquad (20)$$

is the radial coordinate transformed from the interval $[x_b, x_t]$ to the interval $[-1, 1]$, P_n denotes the Legendre polynomial of degree n, and $c_1 \approx -0.207$ and $c_2 \approx -0.097$ are numerically determined constants; for the normalization constant c_0 (cf. Eq. (15)) one then finds $c_0 \approx 0.027$.

Figure 1 shows radial profiles of the mass density, the isotropic and anisotropic magnetic diffusivities, and the effective strength of the $\mathbf{\Omega} \times \mathbf{J}$ effect, and in Fig. 2 the effective strengths of the contributions to the shear-current effect as given by Eq. (8) are displayed. The properties of the two large-scale flows used in the model, namely, contours of the differential rotation rate and the geometry and strength of the meridional circulation, are depicted in Fig. 3. Other model quantities, such as the radial profile of the Coriolis number, Ω^*, and the pumping velocity of the toroidal part of the LSMF, are as in Pipin & Seehafer (2009, see Fig. 2 there).

Numerical procedure

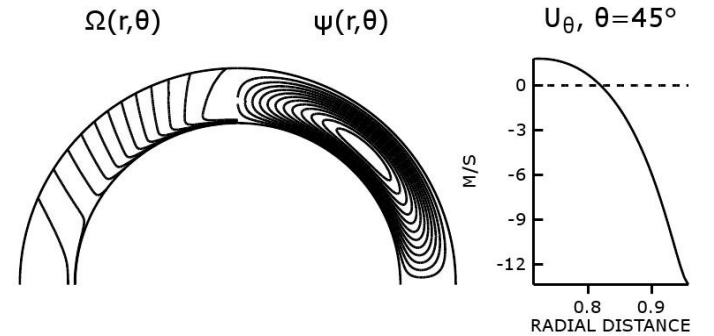In our numerics we use a Galerkin method, expanding the magnetic field in terms of a basis that satisfies the boundary conditions implicitly. The system of Eqs. (2) and (3) admits exponentially growing or decaying solutions, which we represent in the form

$$A(x, \theta, t) = e^{\lambda t} \sum_n \sum_m A_{nm} \sin\theta\, S_{nm}^{(A)}(\xi)\, P_m^1(\cos\theta), \qquad (21)$$

$$B(x, \theta, t) = e^{\lambda t} \sum_n \sum_m B_{nm} S_n^{(B)}(\xi)\, P_m^1(\cos\theta), \qquad (22)$$

where $S_{nm}^{(A)}$ and $S_n^{(B)}$ are linear combinations of Legendre polynomials, and P_m^1 is the associated Legendre function of degree m and order 1. These expansions ensure the regularity of the solutions at the poles $\theta = 0$ and $\theta = \pi$, where B_θ and B_ϕ, i.e., $\frac{A}{\sin\theta}$ and B, have to vanish. The radial boundary conditions are satisfied by the choice (see "basis recombination" in Boyd 2001; Livermore & Jackson 2005)

$$S_{nm}^{(A)}(\xi) = P_{n-1}(\xi) + a_{nm}^{(1)} P_n(\xi) + a_{nm}^{(2)} P_{n+1}(\xi), \qquad (23)$$

$$S_n^{(B)}(\xi) = P_{n-1}(\xi) + b_n^{(1)} P_n(\xi) + b_n^{(2)} P_{n+1}(\xi), \qquad (24)$$

where

$$a_{nm}^{(1)} = \frac{2n+1}{(n+1)^2 + 2m/\gamma}, \quad a_{nm}^{(2)} = -\frac{n^2 + 2m/\gamma}{(n+1)^2 + 2m/\gamma}, \qquad (25)$$

$$b_n^{(1)} = -\frac{x_b(2n+1)}{x_b(n+1)^2 - 2/\gamma}, \quad b_n^{(2)} = -\frac{x_b n^2 - 2/\gamma}{x_b(n+1)^2 - 2/\gamma}, \qquad (26)$$

with $\gamma = \dfrac{2}{x_t - x_b}$ denoting the derivative of ξ with respect to x.

Integrations over radius and latitude, necessary for calculating the expansion coefficients a_{nm} and b_{nm}, were done by means of the Gauss-Legendre procedure, and the eigenvalue problem for determining the exponent λ and the associated eigenmodes
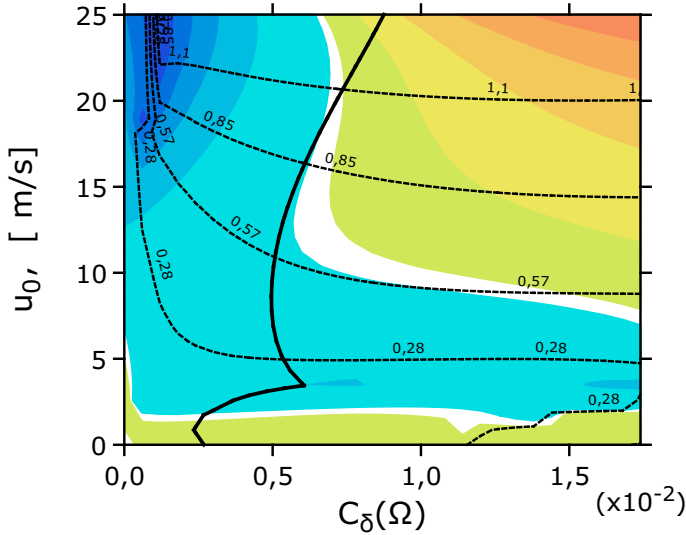
Fig. 4. Difference between the growth rates of the first (most unstable) dipolar mode and the first quadrupolar mode in the plane spanned by $C_\delta^{(\Omega)}$ and u_0 for $C_\delta^{(W)} = 0$. Red colors correspond to a dominance of dipolar modes and blue colors to a dominance of quadrupolar modes. Also shown are isolines of the frequency of the first dipolar mode (in areas where it oscillates), with numbers giving the oscillation frequency ($2\pi/T$, T being the time period of the oscillation) in units of the inverse magnetic diffusion time, $\eta_0/R_\odot^2$. The solid bold line indicates the stability boundary for the first dipolar mode, with the unstable (dynamo) region lying to the right of this line; the first dipolar mode is both unstable and dominating in the upper right quarter of the panel.

was solved by means of Lapack routines. The spectral resolution was 15 modes in the radial basis and 22 modes in the latitudinal basis for the calculations of growth rates (including stability boundaries) and dynamo periods, and 14×30 modes for simulations of time evolutions and butterfly diagrams (see Sect. 3 below); by the assumption of either dipole-type or quadrupole-type solutions the latitudinal resolution could be doubled in a part of the calculations. The results were qualitatively confirmed by a number of runs with still higher resolution. Benchmark calculations for the code used are presented in Appendix A.

3. Results

3.1. $\delta^{(\Omega)}\Omega$ dynamo with meridional flow

The meridional flow becomes essential for the dynamo if the effective magnetic Reynolds number, based on the meridional flow velocity and the turbulent magnetic diffusivity, is high enough. Meridional flow velocities higher than about $10\ldots20$ m/s can scarcely be brought into agreement with the solar observations. Thus, the turbulent magnetic diffusivity should be low. In our formulation, all turbulence effects are consistently scaled by the parameter C_η. Decreasing C_η leads to increasing the influence of the flow on the magnetic field and acts, thus, like increasing the amplitude of the flow. An advection-dominated regime with a solar-like magnitude of the meridional flow is obtained if $C_\eta \lesssim 1/20$. Below, we fix C_η to the value $1/40$.

Figure 4 illustrates the bifurcation scenario for a $\delta^{(\Omega)}\Omega$ dynamo with meridional flow. Here the sources of the dynamo are the $\boldsymbol{\Omega}\times\boldsymbol{J}$ effect (the shear-current effect being neglected) and differential rotation. Also included are turbulent diffusion (isotropic and anisotropic) and turbulent pumping. As the observations of solar activity suggest, the large-scale solar magnetic field is
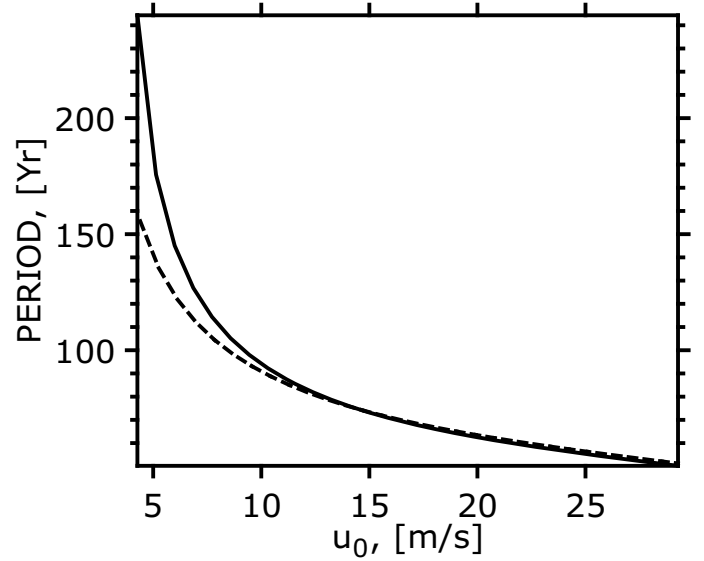

Fig. 5. Dependence of the dynamo period on u_0 along the stability boundary of the most unstable dipolar mode for the $\delta^{(\Omega)}\Omega$ (solid line) and $\delta^{(W)}\Omega$ (dashed line) dynamos.

characterized by an antisymmetric parity with respect to the equatorial plane. In the figure, the plane spanned by the parameters $C_\delta^{(\Omega)}$ (measuring the strength of the $\boldsymbol{\Omega}\times\boldsymbol{J}$ effect) and u_0 (the maximum amplitude of the meridional flow) is displayed, with red/blue colors indicating a dominance of dipolar/quadrupolar modes, which are antisymmetric/symmetric with respect to the equatorial plane, over quadrupolar/dipolar modes. For a sufficiently high velocity of the meridional flow the dipolar parity dominates, as needed for the Sun. The critical dynamo number $C_\delta^{(\Omega)}$ where the first dipolar mode becomes unstable does not depend very much on the flow strength. This may result from the fact that the meridional flow mainly acts as a conveyor belt for the magnetic field, rather than as a generation mechanism.

In Fig. 5 (solid line) the dependence of the dynamo period on the amplitude of the meridional flow along the stability boundary is shown. As expected, the period is a decreasing function of the flow velocity (cf. Bonanno et al. 2002, 2006). The dependence approximately follows a power law with a scaling exponent of -0.7.

Figure 6 (top and middle) shows, in the form of the strength of the toroidal field and field lines of the poloidal field in the meridional plane, the evolution of the LSMF in an $\delta^{(\Omega)}\Omega$ dynamo model on the basis of the first dipolar mode for $C_\delta^{(\Omega)} = 0.006$ and $u_0 = 15$ m/s. In the bottom panel of the figure, an associated simulated butterfly diagram, i.e., the strength of the toroidal LSMF (integrated over depth in the convection zone) in the time-latitude plane is shown, together with isocontours of the radial field component at the top boundary of the considered spherical shell. The latitudinal drift of the toroidal field towards the equator, as indicated by the observations of sunspots, is qualitatively correctly reproduced; the poloidal field is coupled to the toroidal field and shows a similar drift towards the equator. The phase relation between the toroidal and poloidal parts of the magnetic field, in particular the polar reversal of B_r shortly after the maximum of B_ϕ at low latitudes, with $B_r B_\phi < 0$ before and $B_r B_\phi > 0$ after the polar field reversal, is also in good agreement with the solar observations.

In the example shown in Fig. 6, the obtained cycle period is about 80 yr, which is nearly four times the period of the
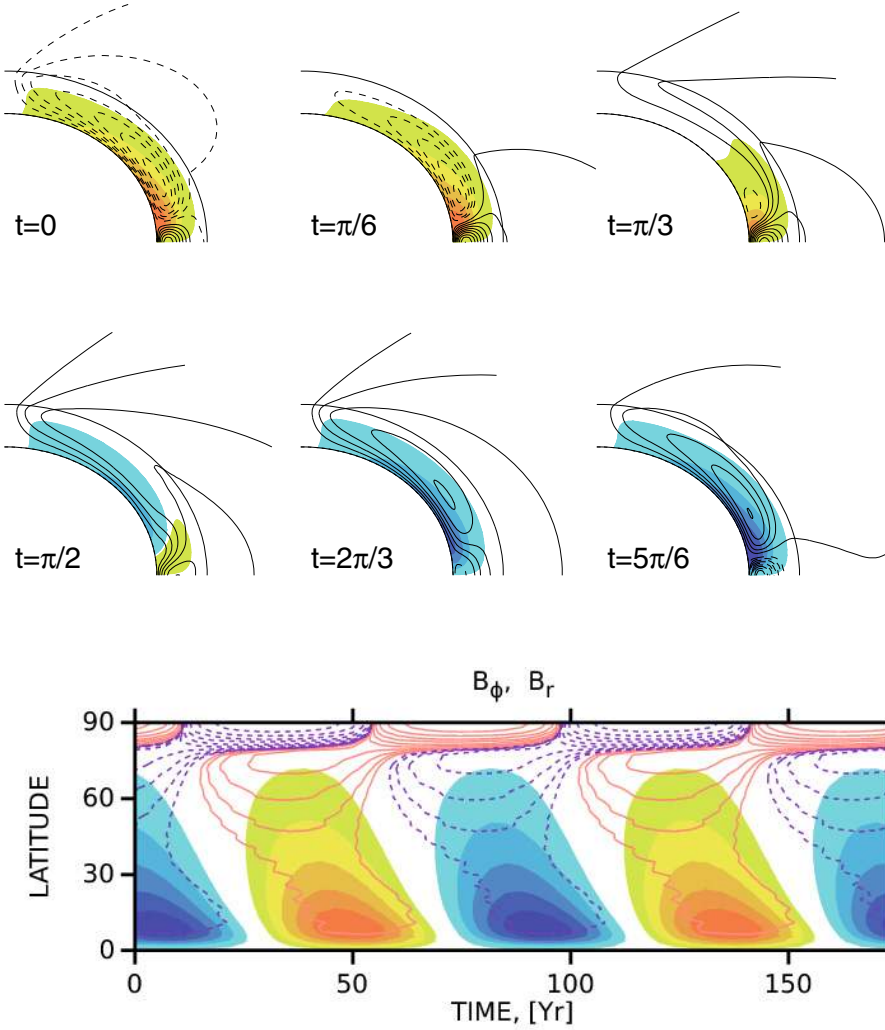
t=0   t=π/6   t=π/3

t=π/2   t=2π/3   t=5π/6

Fig. 6. $\delta^{(\Omega)}\Omega$ dynamo for $C_\delta^{(\Omega)} = 0.006$ and $u_0 = 15$ m/s. *Top and middle*: snapshots of the strength of the toroidal LSMF (color-coded, red/blue colors correspond to positive/negative field values) and field lines of the poloidal LSMF (solid/dashed lines indicate clockwise/counter–clockwise field direction) over half a cycle in the meridional plane. *Bottom*: associated butterfly diagram, showing the (color–coded) strength of the toroidal LSMF (integrated over depth in the convection zone) in the time-latitude plane. Also shown are isocontours of the radial field component at the top boundary (solid red/dashed blue lines indicate positive/negative values).

solar activity cycle. Tuning the parameters cannot significantly reduce the period. This may appear not fully satisfactory, but the period is at least in the right order of magnitude. Furthermore, for the example in Fig. 6, we find $B_\phi/B_r \approx 15$, which is by a factor of $10\ldots100$ smaller than the ratio between the large-scale toroidal and poloidal fields as supposed for the solar convection zone. In general, increasing the speed of the meridional flow in the model reduces the obtained ratio between the toroidal and poloidal fields, in apparent conflict with the need to reduce the cycle period.

3.2. $\delta^{(W)}\Omega$ dynamo with meridional flow

Figures 7 and 8 show results for a dynamo on the basis of the shear-current effect, differential rotation, and a meridional flow, with the α effect and the $\mathbf{\Omega}\times\mathbf{J}$ effect being neglected (but again with turbulent diffusion and turbulent pumping being included). The results strongly resemble those for the $\delta^{(\Omega)}\Omega$ dynamo with meridional flow as described in Sect. 3.1, obviously due to the similarity between the $\mathbf{\Omega}\times\mathbf{J}$ effect and the shear-current effect. The comments given in Sect. 3.1 thus apply here as well. The dependence of the dynamo period on the amplitude of the meridional flow along the stability boundary (Fig. 5, dashed line) approximately follows a power law with a scaling exponent of -0.6.
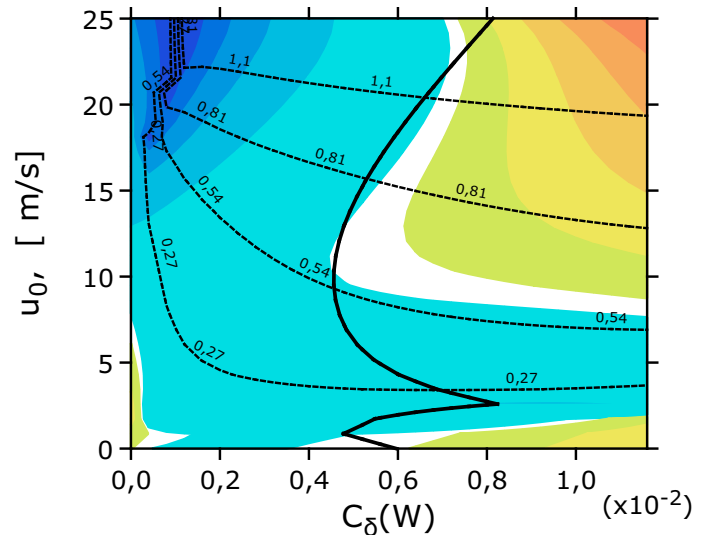

Fig. 7. As Fig. 4, but with $C_\delta^{(\Omega)}$ replaced by $C_\delta^{(W)}$, and $C_\delta^{(\Omega)} = 0$.

4. Conclusions

We have studied kinematic axisymmetric mean-field dynamo models in the geometry of a spherical shell, as appropriate for the Sun and solar-type stars, where the $\mathbf{\Omega}\times\mathbf{J}$ and shear-current
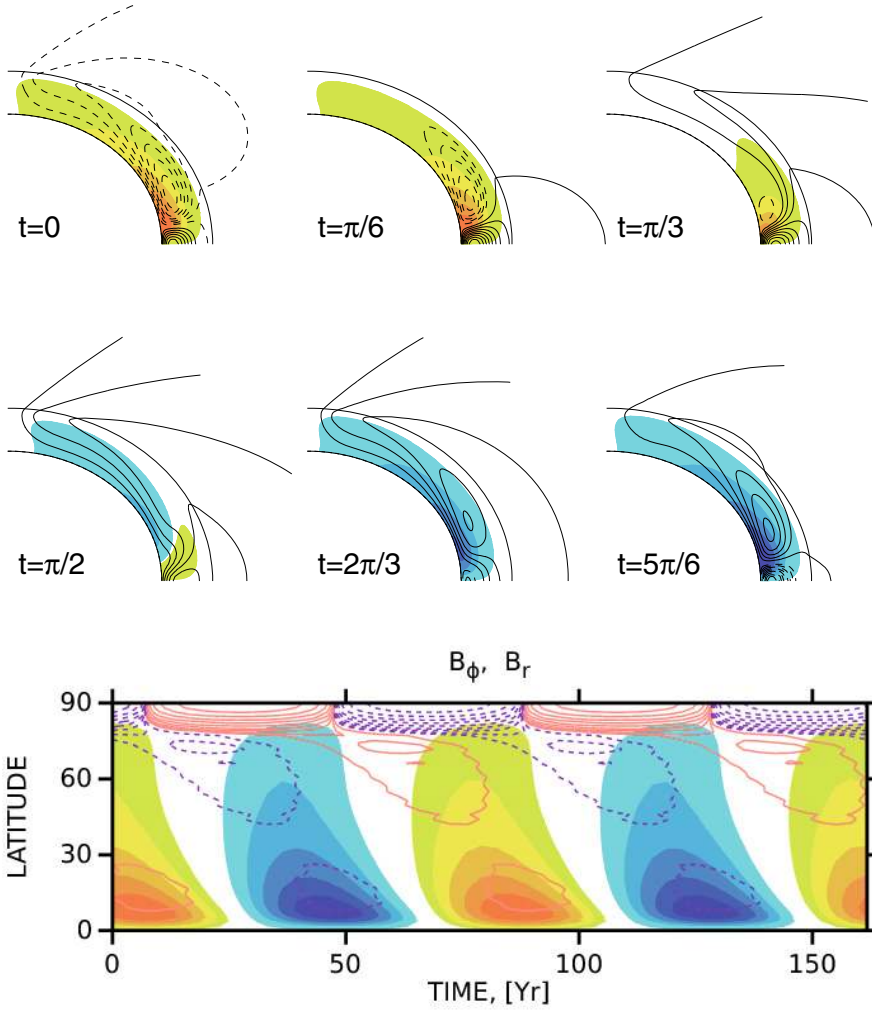
Fig. 8. As Fig. 6, but for a $\delta^{(W)}\Omega$ dynamo with $C_\delta^{(W)} = 0.007$ and $u_0 = 15$ m/s.

effects were included as turbulent sources of the large-scale magnetic field while the α effect was omitted. Besides the turbulent dynamo mechanisms and differential rotation, a meridional circulation, in the form of two stationary circulation cells, one in the northern and one in the southern hemisphere, also was incorporated into the models. We have concentrated on the dynamo onset.

Our results show that the $\mathbf{\Omega} \times \mathbf{J}$ and shear-current effects can, at least in principle, take over the role that the α effect usually plays in mean-field dynamo models. However, only if the meridional flow is sufficiently fast are the characteristic properties of solar-type dynamos qualitatively correctly reproduced. In particular, the amplitude of the meridional flow needs to exceed a threshold value in order that the most unstable magnetic mode has dipolar parity and oscillates. This mode then also shows a latitudinal drift towards the equator within each half cycle and a phase relation between the poloidal and toroidal parts of the field in accordance with the observations of solar activity. The threshold value for the amplitude of the meridional flow, $u_0 \gtrsim 10$ m/s (reached at the surface, the flow speed at the bottom is on the order of 1 m/s), is consistent with solar observations and agrees with the value of 10 m/s often adopted in studies of flux-transport dynamos with the α effect (cf., e.g., Bonanno et al. 2002; Jouve et al. 2008).

In models of advection-dominated dynamos, the specifics of the turbulent dynamo mechanism that generates the mean poloidal field are less important than they are in models without meridional flow (given the rotation law and the generation of the mean toroidal field from the mean poloidal field by velocity shear). Once the field is generated, it is advected equatorwards by the flow. However, the distribution of the turbulent dynamo sources, or their more or less strong localization, decisively influences the parity properties of the LSMF. Studies of flux-transport dynamos with an α effect as the turbulent source of the LSMF indicate that the α effect must be strongly localized at the bottom of the convection zone to ensure the correct (dipolar) parity of the LSMF (Dikpati & Gilman 2001; Bonanno et al. 2002). In our models, the turbulent dynamo effects are distributed over the bulk of the convection zone, though they are strongest near the bottom of the included domain. We note that our turbulent dynamo sources are not introduced arbitrarily but are calculated using a standard model of the solar interior together with rotation rates obtained from helioseismic measurements.

As other advection-dominated dynamo models, the models presented here work only if the effective magnetic diffusivity is strongly reduced compared to the mixing-length estimates. At a radial distance of, say, 0.85 $R_\odot$, the turbulent magnetic diffusivity in our models is about $0.2\,\eta_0$ ($\eta_0 = 1.8 \times 10^9$ m^2/s is the maximum value of the turbulent magnetic diffusivity in the convection zone according to the mixing-length estimate). Together with our value of 0.025 for the parameter C_η (which regulates the turbulence level), this gives an effective magnetic diffusivity of about 10^7 m^2/s, in agreement with the upper limit

of 3×10^7 m^2/s for the turbulent magnetic diffusivity in the bulk of the convection zone given by Dikpati & Gilman (2006, 2007) for flux-transport dynamos with the α effect.

The cycle periods that we obtain are at least three times as long as the observed period of the solar activity cycle. Also, the ratio between the toroidal and poloidal parts of the large-scale magnetic field is significantly smaller than supposed for the solar convection zone (apparently a common problem of all flux-transport models). Here one should keep in mind that requiring a perfect fit to the solar details, as far as these are known, would overstress the models. For instance, a solution that bifurcates at the dynamo onset will change quantitatively if it is traced away from the bifurcation point. Thus, ultimately, self-consistent non-linear models will be needed.

References

Backus, G., Parker, R., & Constable, C. 1996, Foundations of Geomagnetism (Cambridge, UK: Cambridge University Press)
Batchelor, G. K. 1967, An Introduction to Fluid Dynamics (Cambridge, UK: Cambridge University Press)
Bonanno, A., Elstner, D., Rüdiger, G., et al. 2002, A&A, 390, 673
Bonanno, A., Elstner, D., & Belvedere, G. 2006, Astron. Nachr., 327, 680
Boyd, J. P. 2001, Chebyshev and Fourier Spectral Methods, 2nd edn. (Mineola, N. Y.: Dover Publications)
Brandenburg, A. 2005, ApJ, 625, 539
Brandenburg, A., & Subramanian, K. 2005a, Phys. Rep., 417, 1
Brandenburg, A., & Subramanian, K. 2005b, A&A, 439, 835
Brandenburg, A., Tuominen, I., Nordlund, Å., Pulkkinen, P., & Stein, R. F. 1990, A&A, 232, 277
Brun, A. S., & Rempel, M. 2009, Space Sci. Rev., 144, 151
Cattaneo, F., & Hughes, D. W. 2006, J. Fluid Mech., 553, 401
Choudhuri, A. R., Schüssler, M., & Dikpati, M. 1995, A&A, 303, L29
Dikpati, M., & Gilman, P. A. 2001, ApJ, 559, 428
Dikpati, M., & Gilman, P. A. 2006, ApJ, 649, 498
Dikpati, M., & Gilman, P. A. 2007, New J. Phys., 9, 297
Giesecke, A., Ziegler, U., & Rüdiger, G. 2005, Phys. Earth Planet. Inter., 152, 90

Hughes, D. W., & Cattaneo, F. 2008, J. Fluid Mech., 594, 445
Jouve, L., Brun, A. S., Arlt, R., et al. 2008, A&A, 483, 949
Käpylä, P. J., Korpi, M. J., Ossendrijver, M., et al. 2006, A&A, 455, 401
Käpylä, P. J., Korpi, M. J., & Brandenburg, A. 2009, A&A, 500, 633
Köhler, H. 1973, A&A, 25, 467
Krause, F., & Rädler, K.-H. 1980, Mean-Field Magnetohydrodynamics and Dynamo Theory (Berlin: Akademie-Verlag)
Küker, M., Rüdiger, G., & Schultz, M. 2001, A&A, 374, 301
Livermore, P., & Jackson, A. 2005, Geophys. Astrophys. Fluid Dynam., 99, 467
Miesch, M. S., Brun, A. S., DeRosa, M. L., et al. 2008, ApJ, 673, 557
Moffatt, H. K. 1978, Magnetic Field Generation in Electrically Conducting Fluids (Cambridge, UK: Cambridge University Press)
Ossendrijver, M. 2003, A&ARv, 11, 287
Ossendrijver, M., Stix, M., & Brandenburg, A. 2001, A&A, 376, 713
Ossendrijver, M., Stix, M., Brandenburg, A., et al. 2002, A&A, 394, 735
Parker, E. N. 1955, ApJ, 122, 293
Parker, E. N. 1979, Cosmical Magnetic Fields (Oxford: Clarendon Press)
Pipin, V. V. 2008, Geophys. Astrophys. Fluid Dynam., 102, 21
Pipin, V. V., & Seehafer, N. 2009, A&A, 493, 819
Rädler, K.-H. 1969, Monatsber. Dtsch. Akad. Wiss. Berlin, 11, 194, in German, English translation in P. H. Roberts, & M. Stix, Report No. NCAR-TN/IA-60 (1971)
Rädler, K.-H. 1980, Astron. Nachr., 301, 101
Rädler, K.-H. 2000, in From the Sun to the Great Attractor: 1999 Guanajuato Lectures on Astrophysics, ed. D. Page & J. G. Hirsch (New York: Springer), Lect. Notes Phys., 556, 101
Rädler, K.-H., Kleeorin, N., & Rogachevskii, I. 2003, Geophys. Astrophys. Fluid Dynam., 97, 249
Rempel, M. 2005, ApJ, 622, 1320
Rempel, M. 2006, ApJ, 637, 1135
Rogachevskii, I., & Kleeorin, N. 2003, Phys. Rev. E, 68, 036301
Rogachevskii, I., & Kleeorin, N. 2004, Phys. Rev. E, 70, 046310
Rüdiger, G., & Hollerbach, R. 2004, The Magnetic Universe (Weinheim: Wiley-VCH)
Schou, J., Antia, H. M., Basu, S., et al. 1998, ApJ, 505, 390
Schrinner, M., Rädler, K.-H., Schmitt, D., Rheinhardt, M., & Christensen, U. 2005, Astron. Nachr., 326, 245
Schrinner, M., Rädler, K.-H., Schmitt, D., Rheinhardt, M., & Christensen, U. R. 2007, Geophys. Astrophys. Fluid Dynam., 101, 81
Steenbeck, M., Krause, F., & Rädler, K.-H. 1966, Z. Naturforsch., 21a, 369
Stix, M. 1976, A&A, 47, 243
Stix, M. 2002, The Sun. An Introduction, 2nd edn (Berlin: Springer)
Vainshtein, S. I. & Kichatinov, L. L. 1983, Geophys. Astrophys. Fluid Dynam., 24, 273

Appendix A: Benchmarks for the code used

Here we present some benchmark tests for the computer code that we used and show how the crititical dynamo numbers and dynamo periods for the models of Sects. 3.1 and 3.2 converge for an increasing number of modes taken into account.

A.1. Free decay modes

First we test the accuracy of the implementation of the exterior boundary conditions and the speed of convergence. If we neglect all the dynamo effects in Eqs. (2) and (3), only simple isotropic diffusion remains and the equations take the form

$$\frac{\partial A}{\partial t} = \frac{\partial^2 A}{\partial x^2} + \frac{\sin\theta}{x^2} \frac{\partial}{\partial\theta} \frac{1}{\sin\theta} \frac{\partial A}{\partial\theta}, \tag{A.1}$$

$$\frac{\partial B}{\partial t} = \frac{1}{x} \frac{\partial^2 (xB)}{\partial x^2} + \frac{1}{x^2} \frac{\partial}{\partial\theta} \frac{1}{\sin\theta} \frac{\partial (\sin\theta B)}{\partial\theta}, \tag{A.2}$$

where for simplicity the magnetic diffusivity has been assumed to be homogeneous and has been set equal to unity. The equations for the poloidal and toroidal parts of the field are decoupled here. The eigenmodes to Eqs. (A.1) and (A.2) are the free decay modes, exponentially decaying $\propto \exp\lambda_i t$, where the λ_i are the eigenvalues of the Laplacian operator for the considered domain under the imposed boundary conditions; these eigenvalues are all real and negative. For the test, we consider the case of a full sphere (rather than a spherical shell) surrounded by vacuum, for which the free decay modes can be determined analytically and are well documented in the literature (see, e.g., Moffatt 1978; Backus et al. 1996). For that purpose, the potential functions A and B are written as

$$A(x,\theta,t) = e^{\lambda t} \sum_n \sum_m A_{nm} \sin\theta \, S_{nm}^{(A)}(x) \, P_m^1(\cos\theta), \tag{A.3}$$

$$B(x,\theta,t) = e^{\lambda t} \sum_n \sum_m B_{nm} S_n^{(B)}(x) \, P_m^1(\cos\theta), \tag{A.4}$$

with

$$S_{nm}^{(A)}(x) = x\left(P_{2n+1}(x) - P_1(x)\frac{(2n+1)(2n+2)+2(m+1)}{2m+4}\right), \tag{A.5}$$

$$S_n^{(B)}(x) = x\left(P_{2n+1}(x) - P_1(x)\right), \tag{A.6}$$

where the radial variable, x, varies in the interval $[0, 1]$; the transformation to the variable ξ (cf. Eqs. (21) and (22) in Sect. 2) is not used here. By the choice of the basis functions given by Eqs. (A.5) and (A.6) the exterior vacuum conditions are satisfied and the regularity of the fields at the origin is ensured. This set of basis functions differs from that used in our calculations for the spherical shell, but the general structure of the code and the solution algorithms are not changed.

The dependence of the solutions to Eqs. (A.1) and (A.2) on radius is given analytically in terms of the spherical Bessel functions $j_n(x) \propto (1/\sqrt{x})J_{n+1/2}(x)$ (where $J_{n+1/2}$ is the ordinary Bessel function of half-integer order $n + 1/2$), and the decay rates, $-\lambda_n$, are given by the squares of the zeros of the functions j_{n-1} for the poloidal and j_n for the toroidal modes. The slowest decaying (largest scale) poloidal mode decays with the rate $-\lambda_1^{(A)} = \pi^2$, the slowest decaying toroidal mode with the rate $-\lambda_1^{(B)} \approx 4.4934^2$; the corresponding eigenfunctions are $S_1^{(A)}(x,\theta) \propto j_1\left(\lambda_1^{(A)}x\right)\sin^2\theta$ and $S_1^{(B)}(x,\theta) \propto j_1\left(\lambda_1^{(B)}x\right)\sin\theta$. These two decay modes are used for the test. The θ dependences of their potential functions are given by the first terms (with

Table A.1. Convergence of the eigenvalues and eigenvectors of the slowest decaying poloidal and toroidal modes[a].

N	$E(\lambda)[A]$	$E(\boldsymbol{B})[A]$	$E(\lambda)[B]$	$E(\boldsymbol{B})[B]$
3	1.08e-7	3.98e-9	3.83e-5	6.849e-4
4	5.651e-11	1.255e-12	9.984e-8	4.365e-9
5	9.68e-14	2.142e-16	1.207e-10	2.497e-12
6	7.72e-14	2.136e-20	8.707e-14	9.068e-16
7	1.38e-14	1.325e-24	1.77e-14	4.80e-19
8	1.90e-14	4.427e-29	5.32e-15	6.263e-23

[a] N is the number of modes in the radial basis, and $E(\lambda)[A]$ and $E(\boldsymbol{B})[A]$ are the errors of eigenvalue and eigenvector for the poloidal mode and $E(\lambda)[B]$ and $E(\boldsymbol{B})[B]$ the corresponding errors for the toroidal mode.

$m = 1$) in the latitudinal expansions on the right-hand sides of Eqs. (A.3) and (A.4). (The potential functions A and B differ from the potentials S and T in the poloidal-toroidal decomposition $\boldsymbol{B} = \nabla\times(\boldsymbol{r}\times\nabla S) + \boldsymbol{r}\times\nabla T$ as normally used in non-axisymmetric cases, see, e.g., Moffatt (1978) and Backus et al. (1996). For our axisymmetric case, one has $\partial S/\partial\theta = A/\sin\theta$ and $\partial T/\partial\theta = B$. The angular dependence of both S for the slowest decaying poloidal mode and T for the slowest deacaying toroidal mode is given by the spherical surface harmonic $Y_1^0(\cos\theta) \propto \cos\theta$, in agreement with the θ dependences of A and B as given above.)

Table A.1 shows the convergence of the eigenvalues and of the corresponding eigenvectors for our numerical scheme. Similar to Livermore & Jackson (2005), the eigenvectors are scaled so that $S_1^{(A)}(x = 1, \theta = \pi/2) = 1$ and $S_1^{(B)}(x = 0.5, \theta = \pi/2) = 1$, and the errors are measured as $E(\lambda) = |\lambda_{\text{true}} - \lambda_{\text{num}}|$ and $E(\boldsymbol{B}) = \int_V |\boldsymbol{B}_{\text{true}} - \boldsymbol{B}_{\text{num}}|^2 \, dV$. The number of modes in the radial basis, N, is varied, while in the latitudinal basis just the first mode is taken into account. The convergence is seen to be exponential in both the poloidal and toroidal cases.

A.2. Test case B of Jouve et al. (2008)

The next test case is taken from Jouve et al. (2008), who presented a comparitative benchmark study of different numerical codes for axisymmetric mean-field solar dynamo models in spherical geometry. Here we consider their test case B, which is a pure $\alpha\Omega$ dynamo in a spherical shell with sharp gradients of the turbulent magnetic diffusivity and the strength of the α effect at the bottom of the convection zone; for details we refer to Jouve et al. (2008). The potential functions A and B are expanded according to Eqs. (21)–(26) in Sect. 2, and the integration domain is now radially bounded by $x_{\text{b}} = 0.65$ at the bottom and $x_{\text{t}} = 1$ at the top.

In Jouve et al. (2008), the strength of the α effect is regulated by a dynamo number, C_α. The different codes are compared by indicating in tables the critical α-effect dynamo number, C_α^{crit}, at which exponentially growing solutions appear, and the corresponding oscillation frequency, $\omega = 2\pi/T$. In addition, butterfly diagrams and the evolution of the fields in the meridional plane are shown. Our values of C_α^{crit} and ω for different spectral resolutions are given in Table A.2, and Fig. A.1 shows the temporal evolution of the toroidal and poloidal parts of the field (i.e., of the unstable eigenmode) at the critical dynamo number. The values in Table A.2 are in best agreement with those given in the corresponding table, Table 3, of Jouve et al. (2008). Similarly, the evolution shown in Fig. A.1 is apparently identical to that
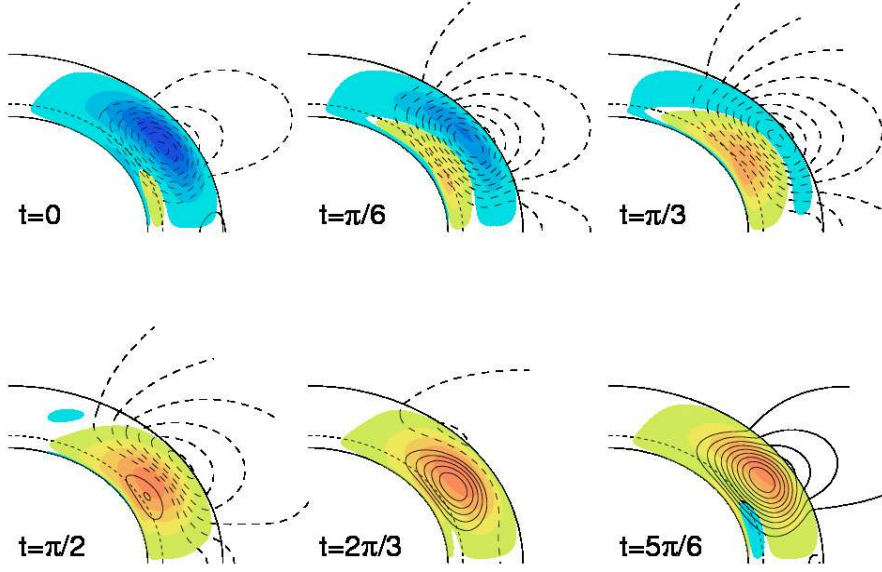
$t=0$ $t=\pi/6$ $t=\pi/3$

$t=\pi/2$ $t=2\pi/3$ $t=5\pi/6$

Fig. A.1. As Fig. 6 (*top and middle*), but for test case B of Jouve et al. (2008) at the critical α-effect dynamo number with a spectral resolution of 16×16 modes.
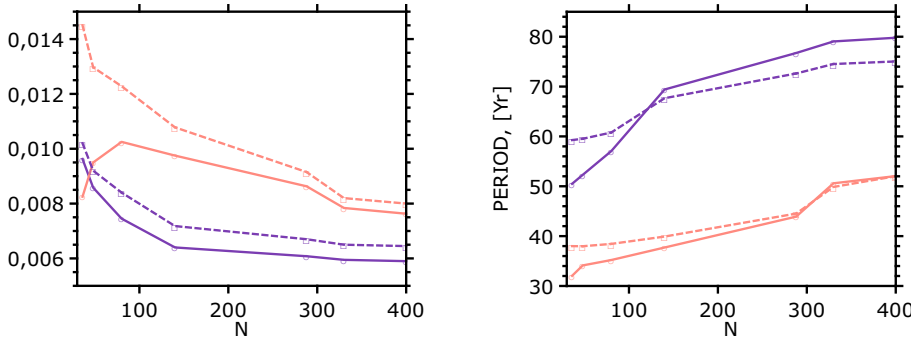
Fig. A.2. Convergence of the critical dynamo numbers (*left*) and associated dynamo periods (*right*) for the models of Sects. 3.1 and 3.2. N is the total number of modes taken into account. Calculations were done for resolutions of 6×6, 6×8, 8×10, 10×14, 16×18, 15×22, and 14×30 modes in the radial and latitudinal bases, respectively (in addition, the dipolar symmetry was taken into account, so that the highest latitudinal resolution is actually 50). Solid lines refer to the $\delta^{(\Omega)}\Omega$ dynamo model and dashed lines to the $\delta^{(W)}\Omega$ dynamo model, and blue color (i.e., the lower/upper curve pair in the left/right panel) corresponds to $u_0 = 15$ m/s and red color to $u_0 = 25$ m/s.

Table A.2. Test case B of Jouve et al. (2008)[a].

Resolution	C_α^{crit}	ω
8×8	0.443	180.5
10×10	0.4175	175.1
12×12	0.4095	172.2
13×13	0.411	172.4
14×14	0.4122	172.7
16×16	0.4125	172.9

[a] Critical values of the dynamo number, C_α^{crit}, and the oscillation frequency at the dynamo onset, ω, for different radial and latitudinal spectral resolutions. ω is measured in units of the inverse magnetic diffusion time.

shown in the corresponding figure, Fig. 7, of Jouve et al. (2008); the same applies to the simulated butterfly diagrams (not shown here).

A.3. Convergence of critical dynamo numbers and dynamo periods for the models of Sects. 3.1 and 3.2

Figure A.2 shows the convergence of the critical dynamo numbers (where the first dipolar mode becomes unstable) and associated dynamo periods for the $\delta^{(\Omega)}\Omega$ dynamo model considered in Sect. 3.1 and for the $\delta^{(W)}\Omega$ dynamo model considered in Sect. 3.2. The amplitude of the meridional flow is $u_0 = 15$ m/s and $u_0 = 25$ m/s; $u_0 = 15$ m/s is the value we used most,

and $u_0 = 25$ m/s is the highest meridional-flow amplitude that we considered, corresponding to the largest magnetic Reynolds number in the study. High Reynolds numbers are known to cause numerical problems.

Appendix B: Definitions of the functions $f_i^{(a)}$ and $f_i^{(d)}$

Here we give the definitions of the functions $f_i^{(a)}$ and $f_i^{(d)}$ that are used in the representation of the turbulent electromotive force $\mathcal{E}$. For details of the calculations we refer to Pipin (2008).

$$f_1^{(a)} = \frac{1}{4\Omega^{*2}}\left[\left(\Omega^{*2}+3\right)\frac{\arctan\Omega^*}{\Omega^*} - 3\right],$$

$$f_3^{(a)} = \frac{1}{4\Omega^{*2}}\left[\left((\varepsilon-1)\Omega^{*2}+\varepsilon-3\right)\frac{\arctan\Omega^*}{\Omega^*} + 3 - \varepsilon\right],$$

$$f_2^{(d)} = \frac{1}{4\Omega^{*2}}\left[\left((\varepsilon-1)\Omega^{*2}+3\varepsilon+1\right)\frac{\arctan\Omega^*}{\Omega^*} - (3\varepsilon+1)\right],$$

$$f_4^{(d)} = \frac{1}{2\Omega^{*3}}\left[\left(2\Omega^{*2}+3\right) - 3\left(\Omega^{*2}+1\right)\frac{\arctan\Omega^*}{\Omega^*}\right].$$